

Experimental investigation of nasal airflow

D Doorly^{1*}, D J Taylor^{1,2}, P Franke¹, and R C Schroter²

¹Department of Aeronautics, Imperial College London, London, UK

²Department of Bioengineering, Imperial College London, London, UK

The manuscript was received on 12 June 2007 and was accepted after revision for publication on 8 October 2007.

DOI: 10.1243/09544119JEIM330

Abstract: The airway geometry of the nasal cavity is manifestly complex, and the manner in which it controls the airflow to accomplish its various physiological functions is not fully understood. Since the complex morphology and inaccessibility of the nasal passageways precludes detailed *in-vivo* measurements, either computational simulation or *in-vitro* experiments are needed to determine how anatomical form and function are related. The fabrication of a replica model of the nasal cavity, of a high optical clarity and derived from *in-vivo* scan data is described here, together with characteristics of the flow field investigated using particle image velocimetry (PIV) and flow visualization.

Flow visualization is shown to be a capable and convenient technique for identifying key phenomena. Specifically the emergence of the jet from the internal nasal valve into the main cavity, how it impacts on the middle turbinate, and the large enhancement of dispersion that accompanies the initial appearance of flow instability are revealed as particularly significant features. The findings from the visualization experiments are complemented by PIV imaging, which provides quantitative detail on the variations in velocity in different regions of the nasal cavity. These results demonstrate the effectiveness of the cavity geometry in partitioning the flow into high shear zones, which facilitate rapid heat transfer and humidification from the nasal mucosa, and slower zones affording greater residence times to facilitate olfactory sensing.

The experimental results not only provide a basis for comparison with other computational modelling but also demonstrate an alternative and flexible means to investigate complex flows, relevant to studies in different parts of the respiratory or cardiovascular systems.

Keywords: nasal airflow, *in-vitro* experiments, particle image velocimetry, flow visualization

1 INTRODUCTION

The nose acts as a remarkably efficient air-conditioning device, performing the primary functions of warming, humidifying, and removing particulate and gaseous pollutants from inspired air before it approaches the delicate structures of the lung. However, the nasal cavity is not designed solely for air conditioning since it also houses the olfactory receptors which provide a sense of smell. To understand how the nose accomplishes its disparate functions, it is necessary to explain how the complex form of the nasal anatomy affects the pattern of nasal airflow under different breathing regimes. The

narrowness of the nasal passageways, combined with their inaccessibility, precludes detailed *in-vivo* measurement using current technology. Furthermore, airways differ markedly between species and thus the validity of animal models is questionable.

Detailed knowledge of how airflow is distributed in the nasal airways and how it is controlled is essential for many applications, which provides motivation for research in this area. Such applications include planning and assessment of surgical interventions, and the design of precision-metered drug delivery systems to target the systemic blood circulation directly through the highly vascularized nasal mucosa.

There have been a number of previous studies which have examined the structure and function of the nose. The anatomy, physiology, and function of the nasal cavity has been described by Mygind and

*Corresponding author: Department of Aeronautics, Imperial College London, Prince Consort Road, London, SW7 2BY, UK. email: d.doorly@ic.ac.uk

Dahl [1], but they did not treat the dynamics of airflow. Naftali *et al.* [2] provided a comprehensive review of *in-vitro*, *in-vivo*, and computational studies of nasal airflow, while Wolf *et al.* [3] compared idealized and replica models of the cavity geometry to model the air-conditioning performance of the nose. Despite these and numerous other studies, the nature of the airflow in the nasal airways is as yet not fully understood, because of the complexity of the anatomy and the development of transitional instabilities at higher flowrates.

The purpose of this paper is to describe the application of *in-vitro* measurements in replica geometries of the human nose derived from *in-vivo* scanning to investigate detailed nasal airflow characteristics. Dye and bubble flow visualization together with particle image velocimetry (PIV) measurements are used to examine the overall character of airflow in the nose, and to quantify how it varies in different regions of the nasal cavity. While this paper deals with nasal airflow, the methodology and the practical issues that are described are relevant to general problems of determining flow in complex anatomical conduits and could be applied to other parts of the respiratory or cardiovascular system.

Anatomically, the nasal cavity is divided bilaterally by a boundary termed the septum which extends from the nares (nostrils) until the nasopharynx; from

there a common airway directs the inspired air towards the larynx. Usually a person does not breathe equally through both sides of the nose at any one time; rather the flow split varies over a period (the 'nasal cycle') according to the relative degree of patency on each side, as reviewed by Eccles [4]. Considering the variation in passageway geometry for a single side of the nose in isolation, inspired air enters the nostril into the nasal vestibule, which is lined with vibrissae (hairs). Air flowing from the nasal vestibule converges until the internal nasal valve, which normally presents the smallest cross-sectional area to the flow. The walls of the nasal vestibule (the alae) are cartilaginous and partly collapse at high inspiratory rates, greatly increasing airway resistance and inducing oral breathing. At lower inspiratory rates, however, the internal nasal valve dominates flow resistance. Immediately after the nasal valve, the cavity expands to a much larger volume. While the total passage area then increases, there are three scroll-like protrusions, namely the superior, middle, and inferior turbinates, which extend into the cavity and limit the overall gain in total area available to the flow. The passageways formed by the air space remaining between these projections are termed meati. The anatomy is shown in a coronal slice derived from a computer tomography (CT) data set (Fig. 1(c)), in which the airways,

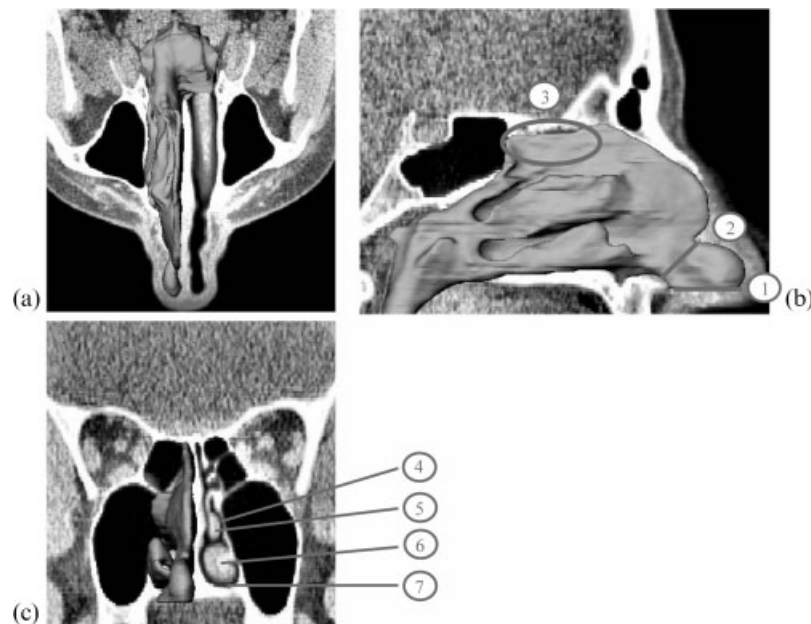


Fig. 1 Unilateral reconstruction of nasal airway, performed in AmiraTM. (a) Single axial CT slice with the reconstructed right nasal airway superimposed. (b) Sagittal CT slice with reconstructed surface superimposed, where the identified features are as follows: 1, nostril; 2, nasal valve; 3, olfactory region. (c) Coronal CT slice with superimposed airway, where the identified features are as follows: 4, middle meatus; 5, middle turbinate; 6, inferior or lower turbinate; 7, inferior meatus

having negligible absorption, appear black. The large voids on each side of the nasal airways are the maxillary sinuses; because the openings or ostia to the sinuses are very small, these and the other sinuses, which can be seen above and behind the airways, are excluded from consideration of the airways.

This paper begins by outlining the major simplifications made in experimental modelling of the nasal airway. Procedures used to create a replica model of the airway anatomy are then described. The experimental technique and practical implementation are considered in detail, before discussing some of the results obtained from a programme of both experimental and computational studies of nasal airflow. The emphasis of the present paper is on the experimental methodology, and the nature of the flow in a single individual geometry, primarily at low flowrates where the flow is laminar. The work reports the initial stage in a programme which encompasses replica geometries from different individuals, and simplified idealized models. How to characterize airway morphological variations, and the effects of such variation on flow and function has been considered by Doorly *et al.* [5] and Taylor *et al.* [6] and will be reported in detail elsewhere.

2 EXPERIMENTAL MODEL CREATION

A fundamental problem in studying nasal airway flow is to decide on an appropriate geometry, since the anatomy displays wide variability, both inter-individually and intra-individually. Inter-individual variations occur in any population, and there are also reported differences in morphology associated with ancestral origin [7]. Intra-individually, the geometry is not fixed but varies with the nasal cycle as mentioned earlier. Thus any *in-vitro* replica model only represents the nasal geometry of an individual for a particular point in their congestion-decongestion cycle. Faced with this, one approach is to produce a simplified airway anatomy [8]. While this has advantages for manufacture, there is a clear risk that arbitrary simplification of the anatomy may neglect certain significant attributes, and hence realistic anatomical models should also be considered.

The starting point for the creation of the replica nasal airway model is a definition of the *in-vivo* geometry derived from CT images. The patient CT data used were obtained with permission by retrospective examination of clinical records from the Ear, Nose and Throat (ENT) Surgical Department at

St Mary's Hospital, Paddington, London. The airway anatomy is determined (by a consultant radiologist) to be normal in a small proportion of ENT patients referred for CT scanning; one such data set was chosen for this study. Given the image data, the process of defining the airway, creating the model, and verifying model accuracy could begin, and the various stages are summarized in the following sections.

2.1 *In-vivo* airway boundary definition

The CT image data set for the airway region consisted of 82 axially acquired images captured to a 512×512 pixel matrix. The image slices were overlapped and acquired with a slice thickness of 1.3 mm and a slice spacing of 0.7 mm, resulting in an in-plane pixel size of $0.39 \text{ mm} \times 0.39 \text{ mm}$. It is impossible to automate fully the process of image segmentation and significant manual user intervention is required for two reasons. First, it is necessary to exclude openings (ostia) to the sinuses to restrict the model domain. Second, with a slice thickness of 1.3 mm, fine dividing structures, particularly in the upper reaches of the cavity, suffer from partial volume effects. This renders unambiguous delineation of boundary contours impossible by simple threshold techniques. By reviewing the airway geometry in both axial and coronal reconstructions as shown in Fig. 1, an operator with knowledge of the basic anatomy can check for consistency and manually exclude false connections apparent at constant threshold levels. The current data set was independently segmented by two operators, leading to slightly different model definitions referred to as models I and II.

Clinically, a coronal acquisition would provide better definition and render the segmentation process simpler. However, axial CT acquisitions are the norm to limit potential damage to the eyes. For the present data set, the use of a more sophisticated approach to image segmentation than provided by simple thresholding might have rendered the process more automated, and it is likely that improvements in CT will in future provide better image resolution via thinner axial slices.

The majority of the results presented were obtained with the geometry definition of model I, shown in Fig. 1, and which possesses the following features.

1. The cross-sectional area of the subject's internal nasal valve was 42 mm^2 . The reported range in

normals is variously quoted as 20–60 mm² [9], 30–40 mm² [10], and 46–115 mm² [11]. The subject nasal valve area is somewhat low, compared with the findings of reference [11] and with other CT data sets that the present authors have examined. This provides a strong jet inflow to the main cavity.

2. The boundary surface is slightly simplified in the upper reaches of the olfactory cleft by removing minor undulations in the roof of the cavity.
3. The lower meatus is only partly patent.
4. The airway is unilateral up to the nasopharynx, i.e. the left nasal airway is excluded, although the nasopharynx is full width.

Practical benefits of a unilateral model are simplified manufacturing process, lower cost, reduced pumping power, and improved optical clarity. Flow visualization results will also be compared with those obtained using model II, where the segmentation of the same subject was performed by a trainee ENT surgeon. Model II differs in that features 2 to 4 are replaced with a fully resolved upper cavity, patent (although narrow) lower meatus, and split (i.e. half-width) nasopharynx respectively. Elsewhere the sectional geometries of the two models are virtually identical (within an image pixel).

Commercial segmentation software (AmiraTM, Mercury Computer Systems, Inc., UK) was used to create the surface definition by delineating the areas of successive images defining the selected nasal passage. In-house smoothing algorithms, developed using the methods of Taubin [12] were applied to remove pixelization artefacts (stair stepping) of the segmentation process. After defining the airway volume of interest, the bounding surfaces were smoothed, and artificial convergent inflow and divergent outflow channels were blended to the model using three-dimensional computer-aided design software (Rhinoceros, Robert McNeel & Associates, USA) to create surface definition files.

2.2 Model fabrication

The intricate flow channels of the nose render most casting processes useless. Previous researchers have employed several techniques to fabricate *in-vitro* nasal cavity models. These include the procedure of Hahn *et al.* [13], who created a 20× scale model by glueing 169 Styrofoam slabs 40 mm thick together. Both Kim and Chung [14] and Hopkins *et al.* [15] created 2× scale transparent models cast around cornstarch rapid prototypes, Hörschler *et al.* [8] used a

transparent resin cast of a 3× scale model, and Häußermann *et al.* [16] created a model constructed from milled consecutive plates.

For this work, a twice-life-scale model was created on a three-dimensional printer (ZPrinter 310, Z Corporation) using the boundary surface definition previously obtained. The model was built up in 0.076 mm layers of a soluble plaster powder, using the surface definition files. After the successive layers had been created, the finished prototype was removed and air-blown to remove adherent powder dust. The porous prototype was sealed with fine layers of poly(vinyl acetate) (PVA), making it impermeable to liquid silicone. This enhanced structural strength and provided a physiologically realistic smooth surface to the model.

The sealed prototype was then placed inside an acrylic box mould which was filled with an optically transparent grade of silicone elastomer (Sylgard 184 silicone elastomer, Dow Corning), previously degassed by exposure to a moderate vacuum. When the silicone was cured, the acrylic box was removed and the model immersed in water to dissolve the prototype and its coating. Final traces of the prototype were removed by continuous irrigation of the flow channels with water, yielding a transparent silicone block encasing the replica nasal airway geometry, as shown in Fig. 2. The flat sides of the acrylic mould afforded a clear optical path for visualization and for PIV studies.

2.3 Model fidelity validation

The silicone phantom was CT scanned (423 images, 512×512 pixel resolution with a slice spacing and thickness of 1 mm and 0.5 mm respectively, resulting in a pixel size of approximately 0.49 mm × 0.49 mm). With the uniform contrast between model and air, and with no extraneous anatomy to be excluded, the images could then be automatically segmented using in-house software. Note that, since the model is twice the *in-vivo* scale, the effective resolution is correspondingly increased, and thus the uncertainty in determining the fabricated model geometry is relatively minor. The reconstruction of the fabricated geometry was then registered to its respective initial computer model, using an iterative closest points algorithm. The mean of the magnitudes of the distances between their surfaces was found to be about 0.29 mm on a 1:1 scale. The error accumulated in the various fabrication stages is thus less than a pixel size of the original data set.



Fig. 2 2× scale flow model created by casting optically clear silicone around a 2× scale plaster powder rapid prototype. The prototype, which was anatomically accurate, had attached inflow and outflow channels and was sealed using PVA to make it impermeable to liquid silicone. After curing, continuous irrigation removed the water-soluble prototype, leaving a rectangular block that contained the nasal geometry

3 EXPERIMENTAL METHODS

The silicone models were connected to a steady flow loop, with flow generated using a constant-pressure-head reservoir. Given the narrowness of the nasal passages, conventional PIV with a single imaging camera is sufficient to provide reasonable quantitative measures of nasal airflow patterns over most of the cavity, provided the potential sources of error (e.g. where the passageways divide into the meati) are recognized. Both the dye filament injection for visualization, and the PIV measurements utilized the same flow loop but different recirculating fluids. Water was chosen for dye visualization as the recirculating liquid needed constant replenishment to ensure the clarity of the liquid and provided reduced modelling flowrates. An aqueous solution of sodium benzoate ($\rho = 1145 \text{ kg/m}^3$; $\nu = 4.29 \times 10^{-6} \text{ m}^2/\text{s}$) with concentration adjusted to match the refractive index of the silicone model (approximately 1.41) was chosen for PIV experiments; this solution also provided relatively low model flowrates compared with equivalent water–glycerine solutions alternatively used for refractive index matching. The effect of refractive index mismatch is depicted in Fig. 3, by imaging a regular grid placed behind the silicone model. As the model is alternately filled with air, water, and aqueous sodium benzoate, the distortion

of the grid is minimized, maximizing the accuracy of the PIV measurements.

3.1 Flow loop

Modelling flowrates were controlled using an orifice valve and flow was driven by a constant-pressure-head reservoir, through the experimental model and exited into a lower reservoir, as shown schematically in Fig. 4. The fluid head was maintained by two parallel pumps (120 series micropump, Michael Smith Engineers) to recirculate the flow back to the upper reservoir; there an overflow assured a constant head height. Diffusers located at the entrance to the reservoir provided damping and minimized the entrainment of bubbles in the flow, which might compromise PIV accuracy. A flow diffuser–straightener combination located upstream of the model inflow ensured unidirectional laminar flow at the model inflow channel.

The flowrate in the model was adjusted according to the circulating fluid to ensure dynamic similarity between the model and the *in-vivo* flow regimes. To characterize the flow, the length scale d used in the definition of Reynolds number

$$Re = \frac{\rho U d}{\mu} = \frac{4\rho Q}{\mu P} \quad (1)$$

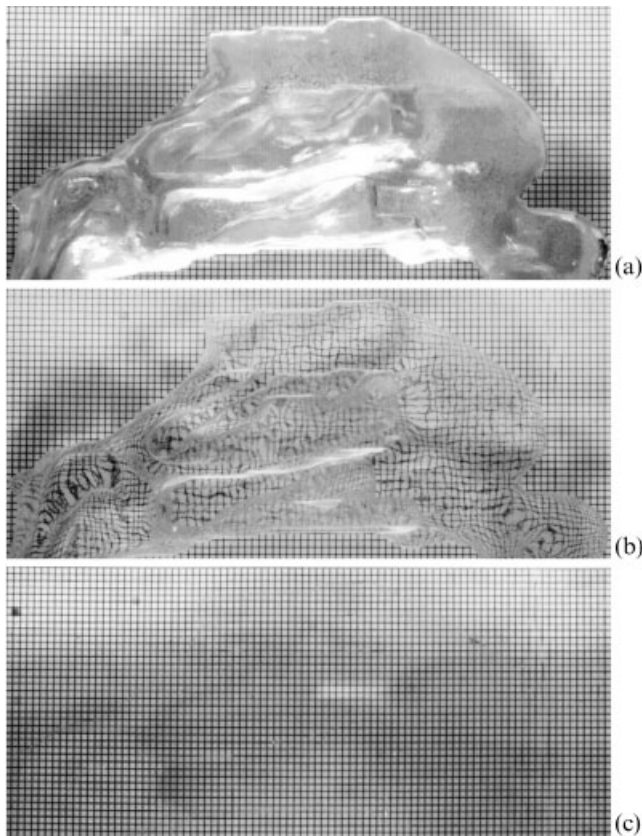


Fig. 3 Photographs depicting the importance of accurate refractive index matching, where the silicone model was placed in front of a regular reference grid to highlight refractive distortion for common recirculating fluids. (a) With air in the passageways, the grid appears totally obscured. (b) With water in the passageways, the grid is visible and distortion varies from low (in the upper planar reaches of the cavity) to severe (where light passes across several interfaces). (c) The near-uniform material properties with aqueous sodium benzoate allow optimal refractive index matching as shown

is the hydraulic diameter at the nasal valve ($d = 4 \times \text{area/perimeter}$, $P = \text{perimeter}$), with μ and ρ representing the fluid dynamic viscosity and density, and the mean flow velocity U deduced from the flowrate Q , at the nasal valve. To match the Reynolds number for the experiment with that *in vivo*, an air flowrate of 100 ml/s corresponds to a flow of approximately 14 ml/s for water and 60 ml/s for aqueous sodium benzoate, using a $2 \times$ scale model. The peak flow velocities in water and aqueous sodium benzoate are thus reduced by a factor of approximately 29 and 7 respectively, which renders imaging far simpler. Nasal airflow is obviously not continuous; however, the respiratory cycle time is very long compared with the mean transit time for

flow through the nose, and steady flow will thus be assumed.

For PIV, the model flowrate was determined by separate multiple PIV acquisitions in the large-diameter inflow tube, before and after the experiments; the results showed negligible variation. Calibration checks performed against a volumetric measurement likewise showed negligible errors. For each acquisition sequence, the temperature, flowrate, and liquid viscosity were measured; the main source of measurement uncertainty arose through viscosity variations with temperature. Summing the overall errors, the uncertainty in Reynolds number was estimated to be ± 4 per cent when a refractive-index-matched fluid was used. Similarly for experiments using water, the maximum uncertainty was estimated to be ± 3 per cent.

3.2 Flow visualization

Neutrally buoyant dyes were metered into the flow through narrow (0.8 mm outside diameter) hollow stainless steel tubes, positioned directly upstream of the nostril. The peak Reynolds number of the external flow around the metering tubes was approximately 17, eliminating the possibility of significant flow disturbance. The buoyancy of the dyes used (Quink Ink, Parker Pen Company) was adjusted with the addition of ethyl alcohol and tested by injection into laminar flow in a horizontal pipe. It was found that the maximum sedimentation velocity was of the order of -0.17 mm/s, which may be considered negligible given typical peak velocities of approximately three orders of magnitude higher for water simulation experiments. The metering rate of the dye filament was controlled using a syringe pump (model 11 syringe pump, Harvard Apparatus), to avoid introduction of flow instabilities. The injected dye filaments were captured at high speed (Vosskuhler HCC-1000, Oxford Lasers) and corroborated with high-resolution still images (Optio 33LF, Pentax). As described in the results section, a limited investigation of bubble flow visualization was also undertaken.

3.3 PIV measurement techniques

The basic procedures for PIV as used in this investigation are summarized next; some of the difficulties experienced are likely to be common to similar investigations in replica geometries. The theoretical basis for PIV imaging, sources of error, practical advice on successful implementation, and

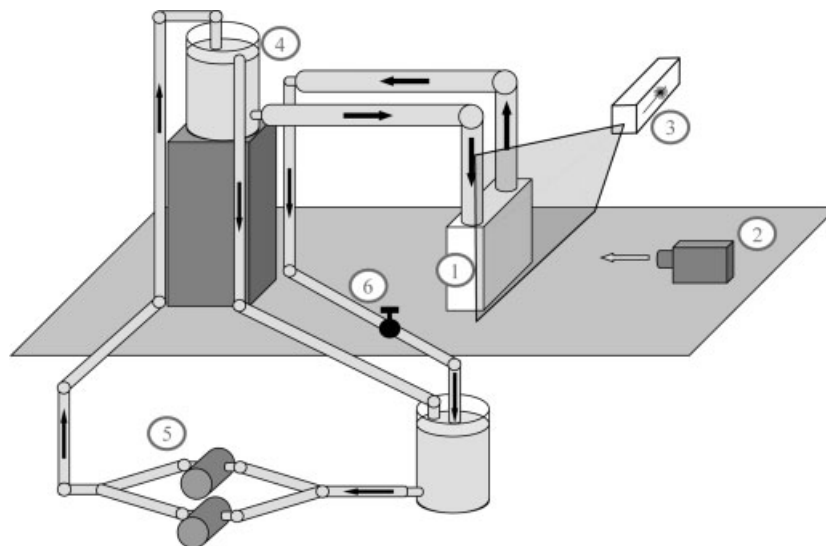


Fig. 4 Schematic representation of the model flow loop used for both dye visualization and PIV: 1, silicone model with inflow section containing a flow straightener and diffuser; 2, digital camera (either high-speed or high-resolution type); 3, diode laser with projected light sheet (for PIV only); 4, constant-pressure-head reservoir, with overflow and diffuser; 5, two parallel pumps recirculating liquid from the lower to the upper reservoir; 6, orifice valve to control the flowrate

refinements to the basic techniques have been well described in numerous texts and papers including those by Keane and Adrian [17, 18] and by Westerweel [19].

In most current implementations, a pulsed-laser light sheet is used to illuminate a plane in the flow, and successive images of minute light-scattering particles are acquired on one or more digital cameras. By dividing the images into interrogation regions, the average particle displacement in each region from one laser pulse to the next can be determined by correlation techniques, and the average velocity in the interrogation region thus inferred. The interrogation region must be large enough to provide good statistical sampling of the imaged particle distribution, while the corresponding spatial extent should be sufficiently small so as to resolve significant small-scale features. Interpolation of the correlation peak generally allows the mean displacement, and hence velocity, to be determined with subpixel accuracy. However, for optimal subpixel estimation, the ratio of imaged particle diameter to detector pixel width should be about 2 [19].

In practice, the achievable measurement accuracy is generally short of ideal, given that the limitations of illumination power, particle size, detector array dimensions, and sensitivity often require compromises. For this work, images were acquired using a VDS Vosskühler HCC-1000 complementary metal-oxide-semiconductor camera. The camera was trig-

gered by a laser pulse controller which drove a 200 W diode laser (16 mJ/pulse, HSI 5000, Oxford Lasers Ltd). Such diode lasers are relatively cheap and afford high repetition rates, although the pulse power is low. To capture the high-speed velocities of the inspiratory jet and reattachment, images were acquired at 462 frames/s, whereas a rate of 115 frames/s was used for the relatively weak recirculation in the inferior meatus. The light sheet was formed through a convex cylindrical lens producing an illumination plane with thickness of less than 0.5 mm about the waist, 150 mm from the laser aperture, with a field of view of typically 65 mm to include the areas of interest. The flow was seeded using 10 µm hollow glass particles (Oxford Lasers) which have a sedimentation velocity of approximately -5.5×10^{-6} m/s in the test fluid. This may be considered negligible given the range of typical velocities (peak, 0.5 m/s) in the flow field for PIV simulations. Given a minimum scaled passage width of the order of 3 mm, the particles can be considered sufficiently small for boundary interference effects to be neglected.

The particle images acquired were diffraction limited, and their imaged size (d_i) at the detector array was calculated to be 0.76 the width of a detector array pixel, from the relation given by [20]

$$d_i = \sqrt{M^2 d_p^2 + d_{\text{Airy}}^2}$$

where

$$d_{\text{Airy}} = 2.44(1 + M) f \# \lambda$$

with d_{Airy} representing the effective diameter of the Airy disc corresponding to the particle imaged through the camera aperture, d_p the size of the seeding particle, M the magnification, $f\#$ the lens f number, and λ the wavelength of the light source. This is well below the optimum, but reducing the field of view to increase imaged particle size limits the extent of the measured flow field. In such circumstances, applying a slight defocus increases the spread of each particle image over the detector array, but the penalty is reduced intensity per imaged particle and this was not employed.

The velocity fields were analysed using adaptive cross-correlation routines to optimize the spatial resolution of the measured velocity fields (VidPIV 4.0g, Oxford Lasers). This method proved particularly useful for the whole field measurements as it allowed the Fourier correlation to use the optimum cross-correlation window displacements to resolve both the high-speed jet and the associated slow

recirculation patterns. Interrogation regions of 64×64 pixels were used with a 50 per cent window overlap for all depicted results except the zoomed PIV measurement of the slow recirculation inside the inferior meatus which used an interrogation size of $32 \text{ pixels} \times 32 \text{ pixels}$, again with a 50 per cent overlap. This was made possible as the low dynamic range of the velocities in this region allowed acquisition at reduced frame rates, allowing increased laser power and particle image size.

4 RESULTS

4.1 Flow visualization (dye filaments in water)

Because of the practical limitations on reservoir size, a non-return water circuit was used for dye visualization experiments. The positions of the filaments will thus appear with slight refractive distortion; nevertheless the positions of critical points such as flow reattachment are not significantly altered.

In Fig. 5(a), dye filament visualization is used to compare the flow in model I (top pair of images), and model II (lower pair).

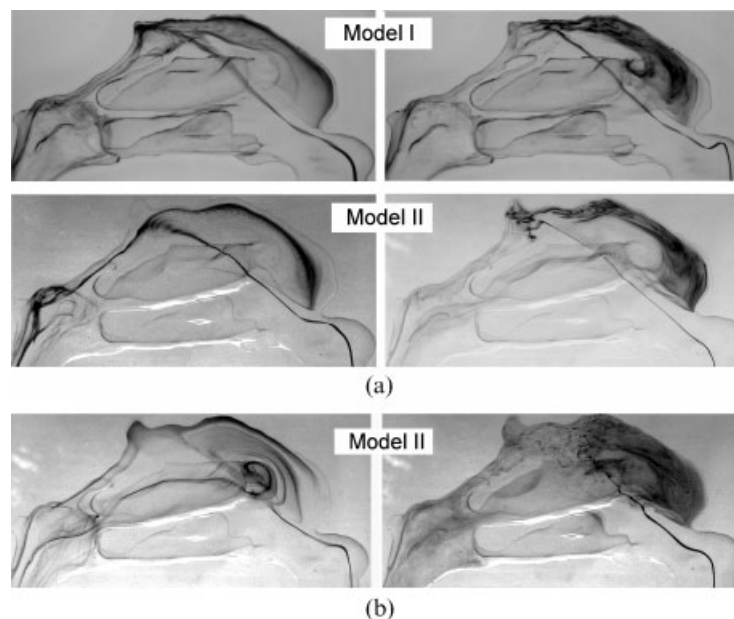


Fig. 5 Dye filament visualization in water representative of steady inspiratory flow in the nasal cavity. (a) Comparison of flow in model I (top row) and model II (second row) at rates equivalent to an airflow of 100 ml/s, $Re = 905$ (left column), and 115 ml/s, $Re = 1041$ (right column). Note slight irregularity in dye filaments near the cavity roof at the higher rate, as interference of the middle turbinate with weak fluctuations in flow amplifies the temporal variability of path lines. (b) Comparison of modelled inspiratory flow in model II at a very low rate of 72 ml/s, $Re = 650$ (left) and at a high rate of 170 ml/s, $Re = 1540$ (right). Note the anterior shift of stagnation point at the low rate, compared with the results at 100 or 115 ml/s. At high flowrates the dye filament shows little disturbance up to interaction with the middle turbinate

images on the left corresponds to a steady inspiratory rate in air for the *in-vivo* nose of 100 ml/s ($Re = 905$), while the images on the right correspond to 115 ml/s ($Re = 1041$). The orientation of the nasal passages has been kept consistent throughout this paper, with flow entering the nose from the nostril at the bottom right in each image, and flowing from right to left.

The olfactory receptors are distributed *in vivo* around the uppermost reaches of the cavity, with the upper boundary of the so-called olfactory cleft corresponding approximately to the nearly flat portion of the cavity roof for model I, and the shallow w-shaped indentation in the cavity roof of model II. In steady quiet inspiration, little flow is directed there, and the lack of mixing means that the injection location has to be positioned carefully.

The images in Fig. 5(a) reveal a similar flow structure in both models at the two flowrates, with the dominant feature being a large recirculation region that occupies the anterior part of the upper cavity. As shown, a portion of the jet inflow directed through the nasal valve reaches nearly to the upper posterior corner of the cavity. There it splits, either slowly flowing all the way back near to where the jet issues from the internal nasal valve or being deflected to exit rapidly the cavity via the nasopharynx.

Considering the results in more detail, first at 100 ml/s, left column of Fig. 5(a), the location of the flow division can be resolved quite accurately using dye visualization, by eye or by video frame analysis. Whereas with model I the dye filament penetrates to the very top of the cavity, in model II the slight crest in the comparable region (which lies anterior to the sphenoidal sinus) is devoid of dye. In the latter case, other tests suggest the crest in the cavity roof is occupied by a small secondary flow recirculation.

Slightly increasing the flowrate to 115 ml/s, right column of Fig. 5(a), reveals slight spontaneous disturbances to the filament stream in both models. The flow stagnation can no longer be so accurately identified from images of filaments introduced at inflow, although its location appears similar, as subsequently confirmed by video frame analysis.

Two other features revealed by the images are worthy of note. First, there is evidence of a vortical structure in the nasal vestibule (producing the twist in the dye filament in the upper right image), as confirmed by bubble visualization, and by computational fluid dynamics studies reported elsewhere. Second, the upper right image shows a centre of the rotation located near the anterior end of the middle turbinate. It suggests that the interaction between

the jet directed through the nasal valve and the middle turbinate is a significant feature and this will be discussed further.

Comparison of the images in Fig. 5(a) shows both that the flow structure in the different models is very similar and that the beginnings of instability occur at similar flowrates. Upstream of the recirculation point the differences in model geometry are small, being effectively confined to the form of the olfactory cleft, and degree of patency of a lower meatus, which is of low calibre. However, downstream of the recirculation, there is an abrupt difference in geometry between models, i.e. a full-width versus a half-width nasopharynx. Neither of these changes produced much discernible effect on the upstream flow; such close similarity in the bounding flowrate for stability was not anticipated.

In Fig. 5(b), dye visualization is shown at considerably lower (72 ml/s, left) and higher (170 ml/s, right) flowrates. Given the correspondence in flow between both models, results are shown for model II alone. At 72 ml/s ($Re = 650$), the flow division is clearly significantly displaced in the anterior direction, with the dye filament observed to splay out as it separates midway along the region expected to contain the olfactory receptors, i.e. bounded on top by the shallow w-shaped undulation anterior to the crest at the rear of the cavity roof.

At a higher inspiratory flowrate of 170 ml/s ($Re = 1540$), perturbations in the jet which impacts on the middle turbinate enhance dispersion of the dye in both anterior and posterior regions of the upper cavity. It is worth noting that, while such rapid dispersion may give the false appearance of a high degree of turbulence, the unsteady impact can greatly amplify time dependence of particle trajectories near a stagnation point. These visualization results are particularly relevant for computational modelling of nasal airflow. The nature of the flow in the cavity, even at higher inspiratory rates, is seen to be predominantly laminar, at least as far as the impact of the inspiratory jet on the middle turbinate; furthermore, relatively weak instability of flow in such a geometry can lead to significant dispersion. The flow instability that develops is seen to originate in the inspiratory jet issuing from the internal nasal valve; the source may be the edge shear layer but the mechanisms are not established by the visualization results. In any event the developing flow instabilities which characterize the flow and are revealed by the visualizations clearly do not conform to the assumptions underlying turbulence models such as the $k-\epsilon$

Reynolds-averaged Navier–Stokes approach, as employed for example in references [21] and [22].

The interception of the jet entering the cavity by the internal nasal valve by the middle turbinate is recognized to play a significant role in nasal function, promoting effective heat and mass exchange [2]. The flow field around the jet impact can be complex, and sensitive to perturbations. Figure 6(a) presents an image from a video sequence of three separate dye filaments (labelled 1, 2, and 3), one of which reaches to the olfactory cleft, for a flowrate of 115 ml/s in model I. Images were captured at 51.3 frames/s using the Vosskühler camera. Two parts of the recirculation are indicated using arrows, with the inner portion centred near the leading edge of the middle turbinate. Slight disturbances in the impact of the jet on the middle turbinate generate splayed finger-like dye projections in the flow spilled from the middle turbinate towards the septal wall. By comparing images which are eight frames apart (about 0.18 ms) (Figs 6(b) and (c)), the slow recirculation of the pattern can be observed, with the relative displacement of identifiable features (e.g. the marker arrow) indicative of pattern rotation rate. Elsewhere in Fig. 6(a), the enhanced mixing of the dye in the olfactory cleft again reveals how variations in the flow impact on the middle turbinate amplify the dispersion of nearby filaments, even though the flow is still essentially laminar.

Considered together, the path lines followed by the three dye filaments (Fig. 6(a)) suggest that the internal nasal valve guides the flow into the main cavity. While a mean flow path cannot strictly be deduced from limited dye filament observations, the suggestion of these and other visualization studies that the mean flow path approximately follows the mid-height of the cavity is confirmed by PIV and other computational studies.

4.2 Flow visualization (microbubbles in glycerol)

Imaging of marker particles can provide more quantitative information than dye visualization. In this investigation, although microbubbles were introduced by a fortuitous difficulty (air entrainment problems when using highly viscous glycerol solutions), they were found to provide an excellent means to highlight the spatial variation in flow velocity throughout the nasal cavity. An example is shown in Fig. 7, where a frame from a sequence recorded at 115 frames/s is shown. Although the flowrate (60 ml/s) is lower than that of greatest physiological interest, essential features of the flow

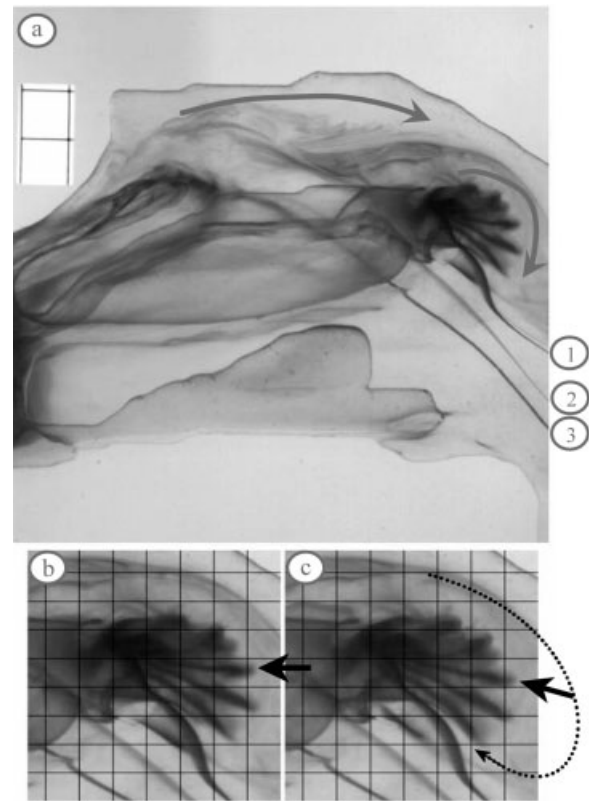


Fig. 6 High-speed dye visualization images depicting flow in the olfactory cleft and the complexity of flow surrounding the impingement and stagnation of the inspiratory jet on the middle turbinate, at an inspiratory rate of 115 ml/s. The paths of the three dye filaments (labelled 1, 2, and 3) are shown in (a), together with arrows representing directions of the two dominant recirculation zones. Magnified sequential images of the persisting regular, although three-dimensional, shedding structure, which are depicted in (b) and (c), are indicative of the enhanced mixing effect resulting from minor variations in the stagnation point location. The regular grid (spacing, about 4.5 mm) was added to aid visualization and the images were taken from a sequence captured at 51.3 frames/s and are approximately 0.18 s apart

are preserved. The rapid flow through the nasal valve produces particle streak images, and zones of slow flow recirculation in the anterior cavity and in the nasal vestibule are clearly identified. Both the main image and dye visualization at a comparable flow (inset) show a more anterior (forward) location of the stagnation point associated with the large recirculation in the upper cavity; this is in line with the preceding results. Physiologically, the location and extent of the recirculating region in the upper cavity are important in affecting the residence time of inhaled species, and consequently for olfaction.

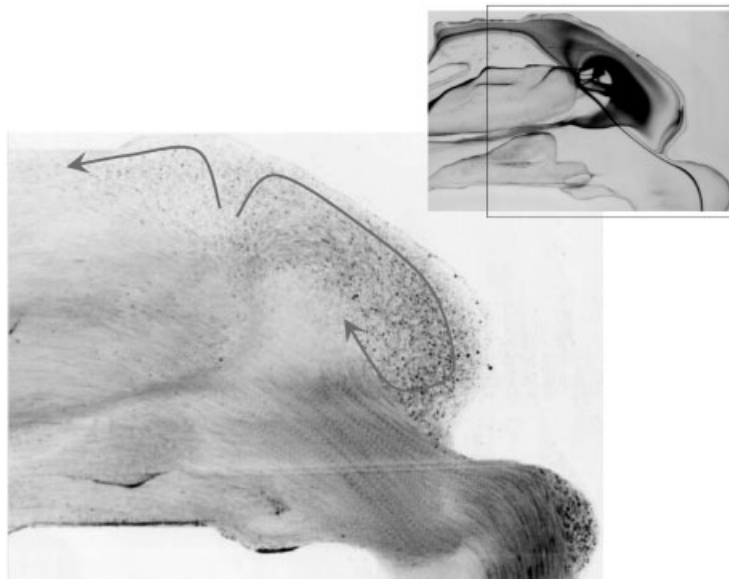


Fig. 7 An image extracted from a multi-pulse (three laser pulses per image) PIV image sequence acquired at 115 frames/s, which has been inverted for clarity. The high-speed jet through the nasal valve is indicated by the bubble streaks, contrasting with the low velocities in the recirculation regions in the upper cavity and at the tip of the nasal vestibule. Note also the change in the position of the recirculation bifurcation point, depicted using the illustrative arrows, in the upper cavity for this flowrate (60 ml/s) compared with that of Fig. 6 (115 ml/s)

Although the technique is promising, it has not been pursued for extraneous reasons (lack of laboratory space for a header tank to drive higher flowrates).

4.3 PIV measurements of nasal airflow

To obtain quantitative estimates of the velocity field in the nasal airway, PIV imaging was applied using the methodology described above, in model I and for a steady inspiratory flowrate of 100 ml/s. Time-averaged velocity fields (average of 511 instantaneous fields) are presented for flow in three regions, illustrating the large variation in velocity in different regions. Velocity magnitude is encoded by grey-scale level and vector length, with flow direction denoted by vector direction and streamlines.

Figure 8(a) shows the measured velocity field in a region encompassing the nasal valve, corresponding to the rectangle indicated on the visualization image in Fig. 8(b). The acceleration of the flow through the nasal valve is evident, with a peak velocity of 3 m/s. The emergence of the jet into the main cavity is shown to be bounded on top by a narrow shear layer between the jet and the adjoining large recirculating region. A magnified view of the shear layer, depicted as a rectangle in Fig. 8(a), is shown in Fig. 8(c).

Close to the nasal valve, the inferior meatus opens out; in this model the entrance along the cavity floor is partly occluded. Velocity field measurements (Fig. 9(a)) show the flow in the region indicated in Fig. 9(b) to be relatively low, and to drive a slow recirculation region. The inspiratory jet (and hence the core flow) thus bypasses this meatus. With a typical peak velocity close to 0.2 m/s, PIV measurements were acquired at 115 frames/s. A magnified view (rectangle in Fig. 9(a)) of the recirculation region is shown in Fig. 9(c).

The dynamics of flow in the roof of the nasal cavity plays a key role in olfaction. PIV measurements are shown in Fig. 10(a), over the region again delineated by a rectangle in Fig. 10(d). As the stagnation and recirculation regions are approached, peak flow velocities decelerate rapidly from 2 m/s to 0.2–0.4 m/s in the apex of the cavity. As indicated by the direction of the velocity arrows, this rapid drop in velocity coincides with flow bypassing the olfactory cleft and does not represent a stagnation of the main inspiratory jet. The streamlines locate the extremity of the large recirculation zone through the olfactory cleft. The long residence times here enable increased mass transfer to the olfactory receptors. A magnified view of the stagnation region, shown as a rectangle in Fig. 10(a), is shown in Fig. 10(b). A minimum intensity projection of this

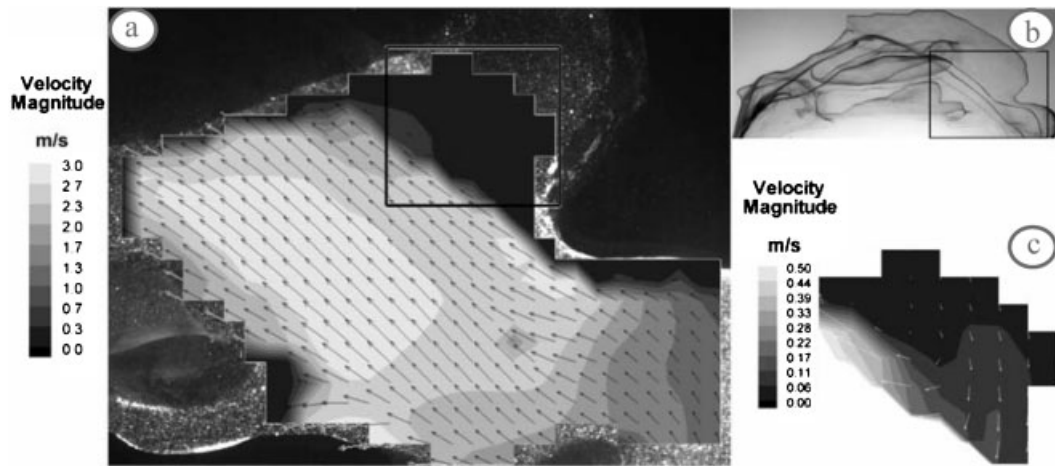


Fig. 8 PIV measurement showing the jet from the internal nasal valve entering the main cavity for an inspiratory rate of 100 ml/s. The field of PIV acquisition is depicted by the rectangle in (b), superimposed on a landmark image. As the flow field accelerates through the nasal valve the acquired velocities, encoded by grey-scale level and vector length shown in (a), are typically 3 m/s. The sudden expansion found as the flow enters the main cavity causes separation and drives the extended recirculation zones shown previously with dye visualization. The range of velocities encountered across the narrow shear layer, which separates the forward jet flow from the adjacent recirculation zone, is indicated in (c) as an enlargement of the smaller subregion of the rectangle indicated in the main image (a)

region was created using the first eight particle images and is shown in Fig. 10(c), where the image has been contrast reversed for clarity. This is similar to a multi-pulse image, and the

streaks show the same patterns of flow division. The streaked image also indicates typical particle density, displacement, and size at the detector array.

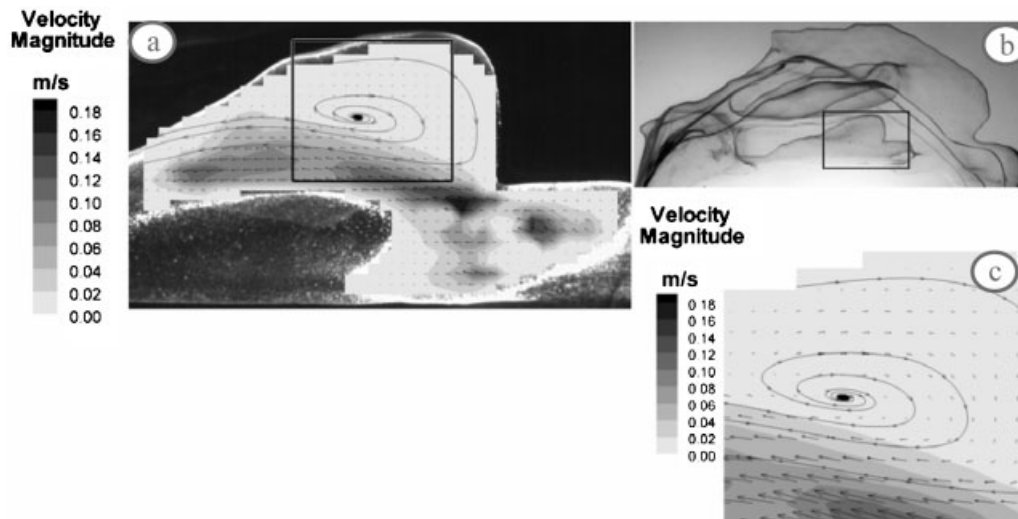


Fig. 9 PIV measurement of flow in the inferior meatus for an inspiratory rate of 100 ml/s. The field of view used for PIV is indicated by the landmark insert (b). Very low flow velocities are recorded in this region, with a significant pocket of very-low-speed recirculating flow, as shown in the detailed view (a). The low velocities in this region afforded PIV acquisition at lower frequency (115 frames/s) in the recirculation region and are replotted in the magnified insert (c)

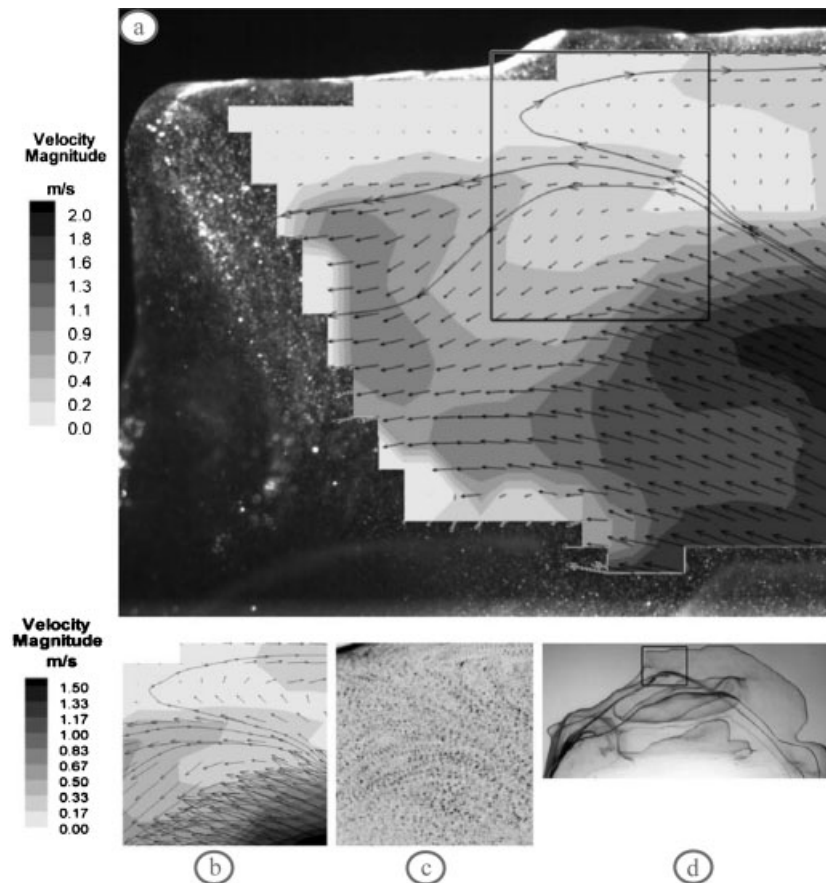


Fig. 10 PIV measurement of flow in the olfactory cleft for an inspiratory rate of 100 ml/s. The rectangle in the landmark image shown in (d) represents the PIV measurement region used for (a). The decelerating flow stagnates at the back of the cavity roof, as shown in (a), and slowly recirculates through the olfactory cleft. The increased residence times, afforded by the slow recirculating velocities, enable efficient mass transfer for olfaction. A magnified view of the stagnation region, which is depicted as a rectangle in (a), is shown in (b). A composite image (a minimum intensity projection of eight sequential images) for the same region is shown in (c), again inverted for clarity

5 DISCUSSION AND CONCLUSIONS

To summarize, the results of experiments using both flow visualization and PIV to investigate nasal airflow have been presented. New results show the sensitivity of the extent of flow recirculation to Reynolds number, the point at which flow irregularity commences, and the very large disparity between the velocity in the region of the nasal valve and that in the upper cleft of the cavity. The visualization results at higher flowrates indicate that the physical flow structure does not correspond to well-developed turbulence; with regard to allied computational simulations, it is evident that the flow does not conform to the assumptions underlying conventional turbulence models. The main cavity flow was found to be relatively insensitive to small inter-observer variations in geometry definition, and to

large changes in the modelled nasopharynx, for inspiratory flow. Procedures to create and validate replica models have been outlined, and the experimental results also serve to illustrate the differing strengths of the measurement techniques for investigations of nasal airflow.

Dye visualization simulations were conducted using water as it was not practical to do so with a refractive-index-matched solution. This was not found to be problematic, since the primary purpose of dye visualization studies was to indicate the flow character. However, dye visualization also provided quantitative detail, since in the upper cleft of the cavity the optical distortion was low and the rear stagnation point of the recirculation zone could be accurately determined by examining dye filament traces. Microbubbles were shown to provide an alternative flow visualization method. When acquired

with a high-speed digital camera, images provided a graphic illustration of the large variations in nasal flow velocity, with the slow recirculating zones in the nasal vestibule and main cavity contrasting with the high-speed jet from the internal nasal valve. Although constraints on the available pumping power limited the use of microbubbles to flowrates below the normal physiological range, this technique, nevertheless, shows considerable promise.

In contrast with the above visualization techniques, PIV with controlled artificial seeding was shown to provide quantitative measurement of flow velocity, with peak velocities of several metres per second in the region of the nasal valve, an order of magnitude greater than velocities in the olfactory cleft.

Overall the results showed that the airflow accelerates in the nasal vestibule, entering the main cavity through the internal nasal valve as a high-velocity jet where it impacts on the middle turbinate. Dye visualization results suggest that the mean flow follows a trajectory corresponding to an arc through the midheight of the cavity. The test models showed either partial or a low degree of patency of the lower meatus, and low flow was found in this region. Low flow was also observed in the olfactory cleft. At low flowrates typical of quiet restful breathing, the flow is laminar, with the beginnings of slight irregularity.

ACKNOWLEDGEMENTS

The authors are indebted to the Biotechnology and Biological Sciences Research Council who funded this research and to Oxford Lasers for their additional support. We are grateful for the assistance and advice of Mr N. Tolley and Dr R. Almeyda of the ENT department of St Mary's Hospital in Paddington, the latter of whom performed the segmentation of model II. The authors also wish to thank the Radiology Department at St Mary's Hospital, London, and Dr Adrian Lee, Mr Alberto Gambaruto, and Mr Nick Watkins for their assistance with this work.

REFERENCES

- 1 Mygind, N. and Dahl, R. Anatomy, physiology and function of the nasal cavities in health and disease. *Advd Drug Delivery Rev.*, 1998, **29**(1–2), 3–12.
- 2 Naftali, S., Rosenfeld, M., Wolf, M., and Elad, D. The air-conditioning capacity of the human nose. *Ann. Biomed. Engng*, 2005, **33**(4), 545–553.
- 3 Wolf, M., Naftali, S., Schroter, R. C., and Elad, D. Air-conditioning characteristics of the human nose. *J. Laryngology Otology*, 2004, **118**(2), 87–92.
- 4 Eccles, R. Nasal airflow in health and disease. *Acta Oto-Laryngologica*, 2000, **120**(5), 580–595.
- 5 Doorly, D. J., Franke, V., Gambaruto, A., Taylor, D. J., and Schroter, R. C. Nasal airflow: computational and experimental modelling. *J. Biomechanics*, 2006, **39**(suppl. 1), S270.
- 6 Taylor, D. J., Doorly, D. J., and Schroter, R. C. Airflow in the human nasal cavity. *J. Biomechanics*, 2006, **39**(suppl. 1), S272.
- 7 Churchill, S. E., Shackelford, L. L., George, J. N., and Blach, M. T. Morphological variation and airflow dynamics in the human nose. *Am. J. Human Biology*, 2004, **16**(6), 625–638.
- 8 Hörschler, I., Meinke, M., and Schroder, W. Numerical simulation of the flow field in a model of the nasal cavity. *Computers Fluids*, 2003, **32**(1), 39–45.
- 9 Lang, J. *Clinical anatomy of the nose, nasal cavity and paranasal sinuses*, 1989, p. 45 (George Thieme Verlag, Stuttgart).
- 10 Proctor, D. F. *The nose, upper airway physiology and the atmospheric environment*, 1982 (Elsevier Biomedical Press, Amsterdam).
- 11 Cakmak, O., Coskun, M., Celik, H., Buyuklu, F., and Ozluoglu, L. N. Value of acoustic rhinometry for measuring nasal valve area. *Laryngoscope*, 2003, **113**, 295–302.
- 12 Taubin, G. A signal processing approach to fair surface design. In Proceedings of the 22nd Annual Conference on *Computer graphics and interactive techniques*, 1995, pp. 351–358 (ACM Press, New York).
- 13 Hahn, I., Scherer, P. W., and Mozell, M. M. Velocity profiles measured for air-flow through a large-scale model of the human nasal cavity. *J. Appl. Physiology*, 1993, **75**(5), pp. 2273–2287.
- 14 Kim, S. K. and Chung, S. K. An investigation on airflow in disordered nasal cavity and its corrected models by tomographic PIV. *Measmt Sci. Technol.*, 2004, **15**(6), 1090–1096.
- 15 Hopkins, L. M., Kelly, J. T., Wexler, A. S., and Prasad, A. K. Particle image velocimetry measurements in complex geometries. *Expl Fluids*, 2000, **29**(1), 91–95.
- 16 Häußermann, S., Bailey, A. G., Bailey, M. R., Etherington, G., and Youngman, M. The influence of breathing patterns on particle deposition in a nasal replicate cast. *J. Aerosol Sci.*, 2002, **33**(6), 923–933.
- 17 Keane, R. D. and Adrian, R. J. Optimization of particle image velocimeters. Part 1: dimple pulsed systems. *Measmt Sci. Technol.*, 1990, **1**, 1202–1215.
- 18 Keane, R. D. and Adrian, R. J. Optimization of particle image velocimeters. Part 2: multiple pulsed systems. *Measmt Sci. Technol.*, 1991, **2**(10), 963–974.

- 19 **Westerweel, J.** Fundamentals of digital particle image velocimetry. *Measmt Sci. Technol.*, 1997, **8**, 1379–1392.
- 20 **Meinhart, C. D. and Wereley, S. T.** The theory of diffraction-limited resolution in microparticle image velocimetry. *Measmt Sci. Technol.*, 2003, **14**(7), 1047–1053.
- 21 **Weinhold, I. and Mylinski, G.** Numerical simulation of airflow in the human nose. *Eur. Arch. Otorhinolaryngology*, 2004, **261**, 452–455.
- 22 **Lindemann, J., Keck, T., Wiesmiller, K., Sander, B., Brambs, H.-J., Rettinger, G., and Pless, M. S.** A numerical simulation of intranasal air temperature during inspiration. *Laryngoscope*, 2004, **114**, 1037–1041.